

High-fidelity simulations of bubble, droplet and spray formation in breaking waves

Zhaoyuan Wang¹, Jianming Yang¹ and Frederick Stern^{1,†}

¹IIHR-Hydroscience and Engineering, University of Iowa, Iowa City, IA 52242, USA

(Received 12 December 2014; revised 22 January 2016; accepted 31 January 2016;
first published online 3 March 2016)

High-fidelity simulations of wave breaking processes are performed with a focus on the small-scale structures of breaking waves, such as bubble/droplet size distributions. Very large grids (up to 12 billion grid points) are used in order to resolve the bubbles/droplets in breaking waves at the scale of hundreds of micrometres. Wave breaking processes and spanwise three-dimensional interface structures are identified. It is speculated that the Görtler type centrifugal instability is likely more relevant to the plunging wave breaking instabilities. Detailed air entrainment and spray formation processes are shown. The bubble size distribution shows power-law scaling with two different slopes which are separated by the Hinze scale. The droplet size distribution also shows power-law scaling. The computational results compare well with the available experimental and computational data in the literature. Computational difficulties and challenges for large grid simulations are addressed.

Key words: computational methods, drops and bubbles, wave breaking

1. Introduction

Air entrainment, bubbles, droplets, jets and spray in breaking waves are of great importance to ship hydrodynamics and ocean engineering. Previous experimental and computational studies are mainly focused on the global structures of wave breaking, such as wave elevation, jet, air cavity and wave breaking processes. The experimental measurements usually can only be done in water due to the technical difficulties, and a detailed description of the energetic wave breaking region is not available. With the development of computational fluid dynamics (CFD) technology, detailed studies of the small-scale structures, such as water droplets and air bubbles, in the two-phase region become possible.

In the CFD studies (Chen *et al.* 1999; Watanabe & Saeki 2002), detailed wave breaking processes and velocity profiles were obtained for plunging wave breaking. The effects of breaking wave intensity on the wave breaking flows were numerically investigated by Iafrati (2009), and detailed quantitative estimates of the drops and bubbles in breaking waves were made using the level-set method in Iafrati (2010). An integrated experimental and CFD study was conducted by Kang *et al.* (2012) and Koo *et al.* (2012) for the plunging wave breaking over a submerged bump with a focus on the overall plunging wave breaking process. The major wave breaking events, such

† Email address for correspondence: frederick-stern@uiowa.edu

as jet plunge, oblique splash, vertical jet and repeated processes were identified. The CFD studies mentioned above were usually conducted on a two-dimensional domain due to the prohibitive computational cost for the three-dimensional simulations. A few attempts have been made of three-dimensional simulations which are focused the three-dimensional vortex structures, energy dissipation and air entrainment (Watanabe, Saeki & Hosking 2005; Lubin *et al.* 2006; Brucker *et al.* 2010; Derakhti & Kirby 2014; Zhou *et al.* 2014; Lubin & Glockner 2015). In the study by Brucker *et al.* (2010), the grid size used was up to 134 million grid points and a scalability study has shown that simulations with 5–10 billion grid points are feasible. In a more recent study by Lubin & Glockner (2015), almost one billion mesh grid points were used to study the fine vortex filaments generated at the early wave breaking stage. In the study by Wang, Yang & Stern (2012a), wave breakings around a wedge-shaped bow and over a submerged bump were simulated using very large grids (1.0–2.2 billion grid points), which was the first attempt to directly simulate the unsteady and energetic wave breaking flows to the scale of micrometres. In order to generate high-resolution two-phase flow data sets for bubble/droplet size distribution for air entrainment and spray formation in breaking waves, further grid refinement is necessary to capture the minimum bubble/droplet size observed in the experiments.

In the experimental study by Cartmill & Su (1993), the bubble size distributions in breaking waves were measured using an acoustic resonator with a bubble radii range of 34–1200 μm . The experimental data for the bubble size distribution are well fitted by a -3 power-law function. Loewen, ODor & Skafel (1996) used a photographic technique for the measurement of the bubble size distributions for bubble radii >0.8 mm. The measured bubble size distributions are well represented by a -3.7 power-law equation. An experimental study by (Deane & Stokes 2002) showed that the bubble sizes are from 2.0 mm down to at least 0.1 mm for the jet plunging period, and larger bubbles from 2.0 to ≥ 10.0 mm are created due to the collapse of the air cavity. The bubble size distribution is separated by the Hinze scale (Hinze 1955), where bubbles larger than the Hinze scale show a $-10/3$ power-law scaling and bubbles smaller than the Hinze scale show a $-3/2$ power-law scaling. The Hinze scale is defined as a length scale below which bubble break up due to turbulent fragmentation ceases. Two different power-law scaling exponents were also observed for the bubble size distributions in the experimental study by Mori & Kakuno (2008). It was found that large bubbles ($d > 3.0$ mm) show -3.4 power-law scaling and small bubbles ($d < 3.0$ mm) show -1 power-law scaling. Tavakolinejad (2010) investigated the bubble size distributions in breaking bow waves using a $2D + t$ technique for bubble diameters ranging from 20 to 2000 μm . Two distinct regions for the bubble size distributions are observed which are separated by $d = 800$ μm . Droplet size distributions for sea spray were studied in Andreas (1998), which surveyed the spray generation functions available in the literature, and a new sea spray generation function for wind speeds up to 32 m s^{-1} was formulated. Recently, a series of experiments for sea spray have been performed by Veron *et al.* (2012) in high wind speed conditions using a photographic method. It has been found that the droplet size distribution is between d^{-3} and d^{-5} for the drop diameters ranging from 196 to 5510 μm . An experimental study of droplets produced by mechanically generated plunging breaking waves was conducted by Towle (2014). Droplet diameter distributions for waves with an amplitude of 0.070 and 0.074 were $d^{-4.68}$ and $d^{-1.50}$ to $d^{-8.79}$, respectively.

The objective of the present study is to validate the predictive capability of the computer code for the bubble/droplet size distribution and investigate small-scale

interface structures in breaking waves, such as bubbles and droplets in air entrainment and spray formation processes, via numerical simulations. This will provide scientific data sets and insights for the wave breaking phenomena and future analysis of bubble dynamics including break up and coalescence. In order to resolve the bubbles/droplets in the breaking waves at the scale of micrometres, high spatial resolution is needed. In the present study, a third-order Stokes wave is used for the wave breaking simulation for the convenience of grid generation and saving computational resources instead of using the bump or wedge as used in Wang *et al.* (2012a). The computational methods and set-up are given in §2. The simulation results and analysis are presented in §3 including a brief discussion of the wave breaking process and 3-D spanwise interface structures, followed by a detailed analysis of bubble/droplet formation and size distributions.

2. Computational methods and set-up

2.1. Computational methods

An orthogonal curvilinear grid solver, CFDShip-Iowa Version 6.2 (Suh, Yang & Stern 2011; Wang *et al.* 2012b), is used for the computations. This solver was extended from the Cartesian grid solver (version 6.1) (Yang & Stern 2009; Wang *et al.* 2009a; Wang, Yang & Stern 2009b) for two-phase incompressible viscous flows with the state-of-the-art numerical methods recently developed at the University of Iowa. In this solver, both gas and liquid phases are considered for the strong interactions between two phases. The level-set-based ghost fluid method is adopted for sharp interface treatment and the volume-of-fluid (VOF) method is used for the interface tracking. A brief description of the numerical methods are given below, and details can be found in the papers given herein.

A finite difference method is used to discretize the Navier–Stokes equations on a non-uniform staggered orthogonal grid. Time advancement of the present study is based on the semi-implicit four-step fractional step method (Choi & Moin 1994). The diagonal diffusion terms are advanced with the second-order Crank–Nicholson method and the other terms by the second-order explicit Adams–Bashforth method. The convective terms are discretized using third-order QUICK (Leonard 1979) and fifth-order WENO (Jiang & Shu 1996) schemes. Semi-Lagrangian advection schemes for the Navier–Stokes equations are also implemented to increase the maximum allowable time step. All other terms are discretized with the standard second-order central difference scheme. The pressure Poisson equation is solved using the HYPRE library (Falgout, Jones & Yang 2006).

An accurate and robust new VOF method developed by Wang, Yang & Stern (2012c) is used to solve the VOF advection equations. The interface normal vector is evaluated using a signed distance function obtained from a second-order distance function construction scheme. A novel technique for the calculation of the normal vector is developed, which is very robust and accurate, especially for the under-resolved regions. A semi-Lagrangian advection scheme for the VOF method (Wang, Yang & Stern 2012d) is used to eliminate the time step constraints due to the CFL condition and to speed up the computations. As a combined Eulerian and Lagrangian method, the semi-Lagrangian method is unconditionally stable and also maintains the efficiency of the Eulerian method.

The code parallelization is done via a domain decomposition technique using the MPI library. A simple domain decomposition technique is used in all three directions which facilitates the use of thousands of processors, even with coarse grids. Parallel

I/O using MPI2 have been implemented (Yang *et al.* 2008) such that all processors read from and write to one single file simultaneously, which is much more effective than one or a few processors receiving data from all processors and writing to one or a few files. This is critical for simulations using billions of grid points since the memory of a few processors is insufficient to handle such huge data sets. Numerous numerical tests and application examples have been performed to verify and validate the code such as a static drop in equilibrium for surface tension modelling, a small-scale single bubble rising in quiescent water, droplet impact onto a liquid pool and plunging wave breaking (Yang & Stern 2007, 2009; Wang *et al.* 2009a,b; Suh *et al.* 2011; Koo *et al.* 2012; Wang *et al.* 2012a–d). The accuracy, robustness and efficiency of the numerical methods especially for interface tracking, sharp interface treatment and surface tension modelling have been extensively verified.

2.2. Computational set-up

The computational conditions and physical parameters are similar to those used in the 2-D studies by Chen *et al.* (1999), Iafrati (2009, 2010) and Wang *et al.* (2009a). The wave profile is initialized using the following function

$$\eta(x, 0) = \frac{1}{2\pi} \left(\epsilon \cos(2\pi x) + \frac{1}{2} \epsilon^2 \cos(4\pi x) + \frac{3}{8} \epsilon^3 \cos(6\pi x) \right), \quad (2.1)$$

where $\epsilon = 0.55$ is the wave slope. The wavelength λ is used as the reference length and the reference velocity is chosen as $U_r = \sqrt{g\lambda}$. The Weber number is $We = \lambda \sqrt{g\rho_w/\sigma} = 100$ and the Reynolds number is $Re = \rho_w g^{1/2} \lambda^{3/2} / \mu_w \simeq 4.4 \times 10^5$, where g is the gravity acceleration, ρ_w is the water density, σ is the surface tension coefficient and μ_w is the water viscosity, which correspond to a water wave with a wavelength of 27 cm.

Three different grids were used for the computations with a minimum grid spacing of 0.264 mm, 0.132 mm and 0.065 mm (see table 1), respectively. The computations for the coarse and medium grids were carried out in a 3-D domain of $[-0.5\lambda, 0.5\lambda]$, $[0, 0.5\lambda]$ and $[-0.5\lambda, 0.5\lambda]$ in the streamwise, spanwise and vertical directions, respectively. For the fine grid case, the spanwise dimension was reduced to $[0, 0.25\lambda]$ in order to save computational resources. Uniform grid spacing was used in the streamwise and spanwise directions. In the vertical direction, uniform grid spacing was used for $-0.25\lambda < z < 0.25\lambda$ and the grid spacing gradually increased below $z = -0.25\lambda$ and above $z = 0.25\lambda$. Periodic boundary conditions were imposed in both streamwise and spanwise directions and the slip boundary conditions were applied in the vertical direction. Constant time steps were used for the three grids as shown in table 1. The time was non-dimensionalized by $t_r = \sqrt{\lambda/g}$. The simulations were started at time $t = 0.0$ with the velocity in the liquid phase initialized using the velocity potential and the air phase at rest. For the fine grid, the 2-D results (wave profile and velocity field before plunging) were used as the initial conditions.

There are many challenges and difficulties for simulations using huge grid sizes (billions of grid points), such as data transfer and storage, data visualization, analysis and animation. In the present study, a high priority queue was requested and approved by the US DoD Supercomputing Resource Centers (DSRC) with 4 and 11.2 million CPU hours for FY2013 and FY2014, respectively. This is critical to obtain enough processors and avoid unacceptable waiting time in the queue to speed up the computations, and also to facilitate data post-processing using HPC job based software in parallel mode.

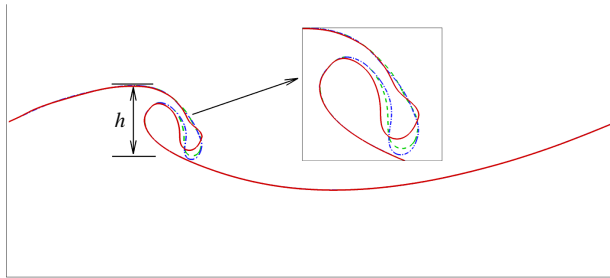


FIGURE 1. (Colour online) Comparison of the wave profiles of the three different grids at $t = 1.25$: coarse grid (solid line), medium grid (dashed line) and fine grid (dash-dotted line). h is the height of wave breaking region, which will be used to calculate the energy dissipation rate in § 3.4.

Simulations	Grid ($x \times y \times z$)	Δh_{min} (mm)	Spanwise (y)	Time step
Coarse	$1024 \times 512 \times 768$	0.264	0.5λ	1.0×10^{-4}
Medium	$2048 \times 1024 \times 1536$	0.132	0.5λ	1.0×10^{-4}
Fine	$4096 \times 1024 \times 2816$	0.065	0.25λ	2.5×10^{-5}

TABLE 1. Simulation configurations for the coarse, medium and fine grids.

Simulations	Grid size	Errors
Coarse	$1024 \times 512 \times 768$	N/A
Medium	$2048 \times 1024 \times 1536$	2.03×10^{-3}
Fine	$4096 \times 1024 \times 2816$	9.71×10^{-4}

TABLE 2. Relative errors of the interface location between the consecutively reduced grid spacing at $t = 1.25$.

Computational results for the overturning jet before wave plunging on the three grids are shown in figure 1 for grid convergence studies. Similar grid studies for the wave breaking simulations can be found in Wang *et al.* (2009a) and Brucker *et al.* (2010). The overall structures of the interface obtained on the three grids are similar. The jet tip is slightly thinner and sharper on a fine grid than on a coarse grid since a fine grid can capture more details of the interface structure. The relative errors of the interface location are evaluated by using the L_1 norm (Wang *et al.* 2009b), as shown in table 2. As shown in the table, the relative error decreases with grid refinement, which indicates the convergence of the computational results. As discussed in Chen *et al.* (1999) and Lubin *et al.* (2006), grid convergence analysis is quite difficult for this kind of flow which is characterized by unsteady air–water interface breaking. Although smaller interface structures can be resolved with higher grid resolution, the overall flow dynamics of wave breaking is not much affected by the small interface structures. The results computed on the medium grid are used for the following discussions unless otherwise stated.

The kinetic (E_k), potential (E_p) and total (E_t) energies of the wave breaking are evaluated according to the formulations given in Chen *et al.* (1999) and Iafrati (2009). The time histories of the kinetic, potential and total energy for the coarse and medium

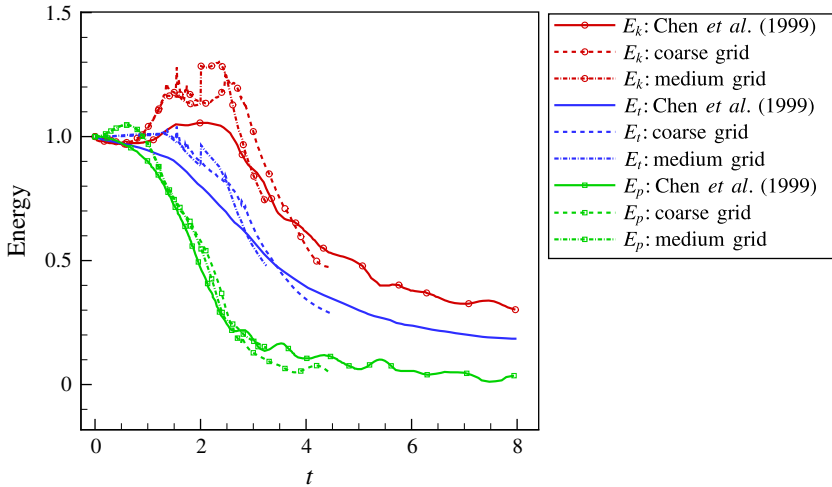


FIGURE 2. (Colour online) Time history of total wave energy (E_t), kinetic energy (E_k) and potential energy (E_p).

grids are shown in figure 2 along with the 2-D computational results by Chen *et al.* (1999). The results are non-dimensionalized using their initial values and the time is non-dimensionalized using the time scale given above. As shown in the figure, the present simulation results for the two grids are almost identical at the early wave breaking stage. After approximately $t = 1.5$, fluctuations can be observed in the kinetic energy, whereas both the total and potential energies are still very close. As compared to the results by Chen *et al.* (1999), the energy time histories exhibit similar trends. The kinetic energy in the present simulations shows a higher jump after jet plunges, which can also be found in the results of Lubin *et al.* (2006). The total energy of the present simulations is also higher than that of Chen *et al.* (1999) and slightly rises before plunging. A similar trend can be found in figure 16 of Lubin & Glockner (2015). This is because the Reynolds number used in the present study is much larger than that used in Chen *et al.* (1999). Besides the higher Reynolds number, some other effects, such as the larger viscosity and density ratios (water/air), 3-D computation, much finer grid and higher-order convection schemes, are also responsible for the differences. As for the potential energy, the present simulation results are very close to Chen *et al.* (1999) except that a bigger rise can be found when wave crest reaches the maximum height in the present simulation.

The water–air interface is extracted from the level-set function and the bubbles/droplets are identified from the VOF function. The identification of the bubbles/droplets is performed using a non-recursive neighbour searching algorithm. A multi-block identification procedure (Herrmann 2010) is employed to handle bubbles/droplets shared by different blocks. The volume of each bubble or droplet is obtained from the VOF function and an equivalent spherical diameter is then calculated. A close-up view of the droplets in the breaking wave is shown in figure 3, where the minimum droplet size that is captured is less than one grid spacing. These under-resolved bubbles/droplets will not be counted due to numerical errors. The numerical errors of VOF interface reconstruction can be significant when the bubble/droplet size is comparable to the grid spacing. As noted by Li *et al.* (2010), serious advection errors will be introduced when the liquid structure is less than twice

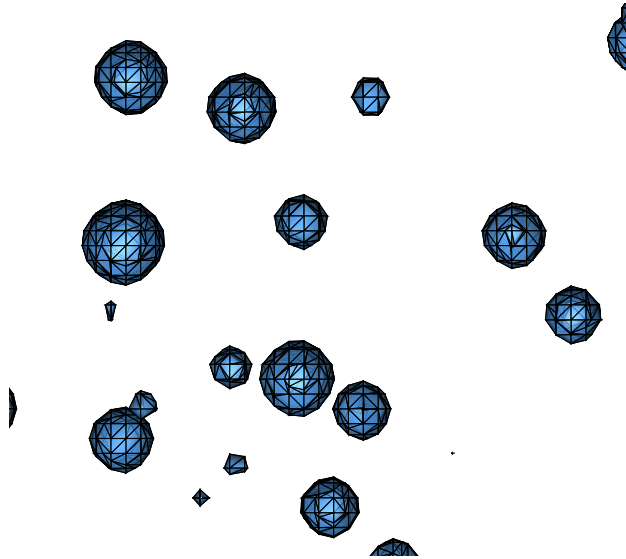


FIGURE 3. (Colour online) Close-up view of the droplets in wave breaking.

the grid spacing. As shown in figure 7.3 of Clift, Grace & Webber (1978), when the diameter is $d < 1.0$ mm, the surface tension force is dominant and the shape of bubble/droplet lies in the spherical regime. As shown in figure 3, with more than 4 computational cells (0.53 mm) per bubble/droplet diameter, the droplets/bubbles take on a spherical shape. Herein, bubbles/droplets are considered as unresolved and will not be counted when their diameters are less than 5 computational cells. It should be noted that the small under-resolved bubbles/droplets are different from the so-called ‘flotsam’ or ‘jetsam’ which are bigger in size and mainly appear in the lower-order VOF schemes and algebraic methods (Aulisa *et al.* 2003). The VOF/PLIC scheme, as used in the present study, is more accurate and does not produce the so-called ‘flotsam’ or ‘jetsam’ (Scardovelli & Zaleski 2003).

3. Results and analysis

3.1. Wave breaking process

The snapshots of the time sequence of the wave breaking process are presented in figure 4. More details of the wave breaking process are shown in the supplementary movie 1 available online at <http://dx.doi.org/10.1017/jfm.2016.87> with side view, perspective view and close-up view of the plunging region. The water–air interface is identified using the isosurface of the zero distance function. Droplets and bubbles are shown above and below the free surface, respectively. It is hard to tell the difference of the bubble and droplets from the figure. It is difficult to assign a different colour for water and air using the extracted isosurface to represent the interface. Different colours can be used if the phase function (distance function in present study) in the whole domain is plotted, but this is currently not feasible for the post-processing software to handle since the grid size is so large.

The wave breaking processes shown in the figure include the formation of the maximum wave height, overturning jet, wave plunging, splash ups and subsequent wave breaking events. Figure 4(a) is for $t = 0.56$ when the wave crest becomes

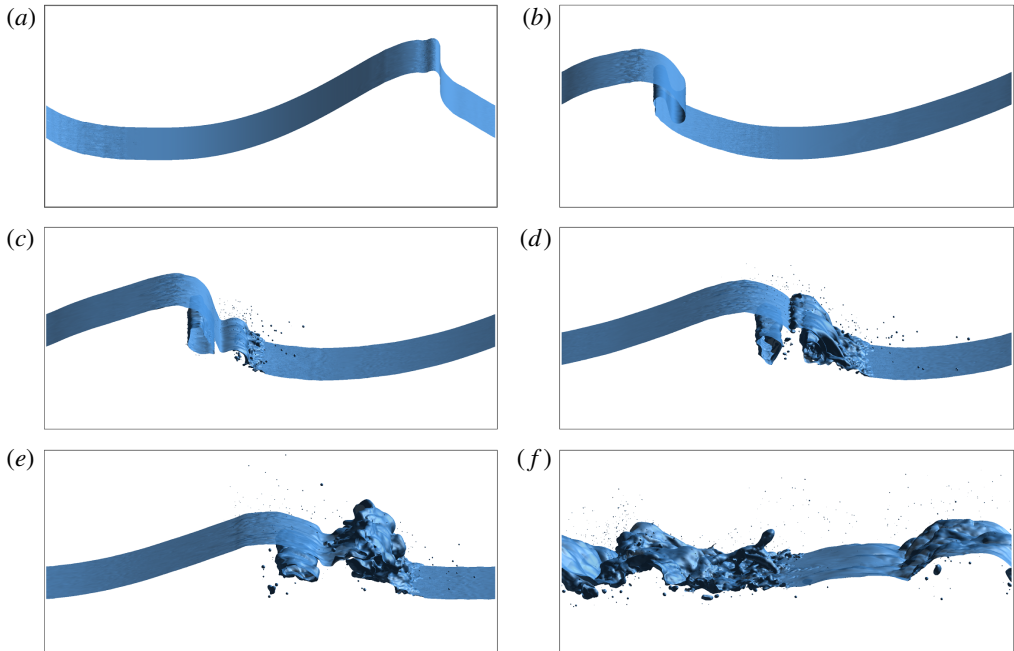


FIGURE 4. (Colour online) Time sequences of Stokes wave breaking. (a) $t = 0.56$; (b) $t = 1.20$; (c) $t = 1.44$; (d) $t = 1.76$; (e) $t = 2.08$; (f) $t = 2.96$. The blue surface is the air–water interface identified using the isosurface of the zero distance function, which is the same as in figures 5, 10 and 11.

steepest and reaches its maximum height. Figure 4(b) shows the overturning jet. The plunging jet shoots out from the wave face, falls and touches the wave trough with an air tube entrained, as shown in figure 4(c). The cross-section of the entrained air tube has a roughly elliptical shape. The plunging jet rebounds off the wave trough forming the splash up, which subsequently grow and fan out (see figure 4d). As the original wave crest decreases in height, a vertical jet is being formed with increased height, as shown in figure 4(e). The entrapped air tube continues to be deformed and eventually collapses and the vertical jet plunges forward after it reaches the maximum height, and the wave breaking enters the subsequent process with successive splash ups with reduced energy and chaotic flow motion. The major wave breaking events are in very good agreement with the 2-D simulations conducted by Chen *et al.* (1999). Detailed comparison with the results in Chen *et al.* (1999) for 2-D simulations has been made in the previous study by the authors (Wang *et al.* 2009a).

3.2. 3-D interface structures

Figure 5 shows the wave profile at time $t = 1.76$ when the splash ups are being generated after the initial jet plunges. The 3-D local interface deformation in the spanwise direction is clearly demonstrated in figure 5(b). These transient rib-like interface structures are also observed in the studies by Watanabe *et al.* (2005) and Saruwatari, Watanabe & Ingram (2009), which are related to vortex structures beneath the interface. The 3-D vortex structures are identified using the Q -criterion which are shown in figure 6. Q is the second invariant of the velocity gradient (Jeong &

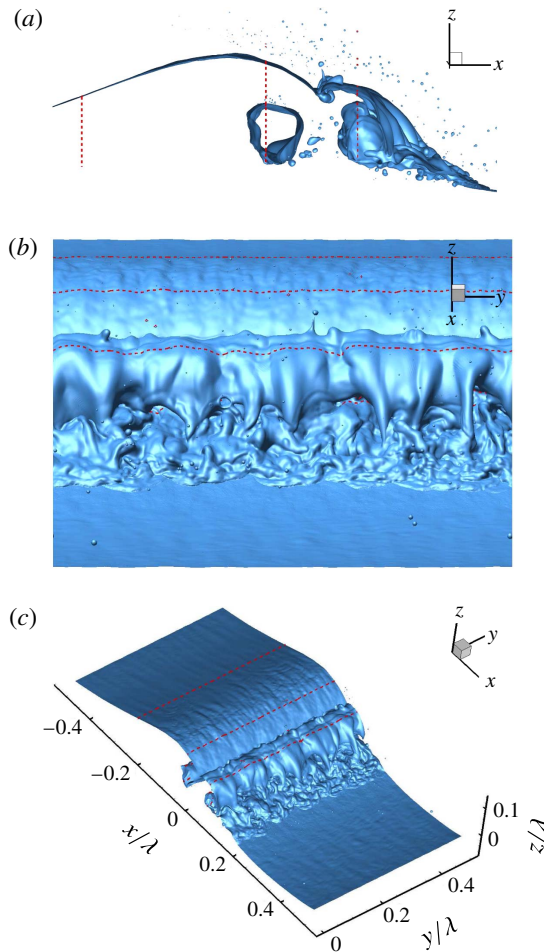


FIGURE 5. (Colour online) Wave profile of simulation at $t = 1.76$. (a) Side view; (b) front view; (c) perspective view: the dashed line shows the cross-section slice locations at $x/\lambda = -0.25, -0.05$ and 0.05 .

Hussain 1995) and represents the balance between shear strain rate and vorticity magnitude, which is more useful to identify vortices for complicated 3-D flows than the vorticity contours. In figure 6(a), Q isosurfaces are plotted for both air and water phases along with the air–water interface. It can be seen that strong organized structures with streamwise vortex filaments are wrapping around a major spanwise vortex tube in the upstream air phase. In order to show the vortex structures beneath the interface, Q isosurfaces are only plotted for the water phase with the interface removed in figure 6(b). As shown in the figure, streamwise vortex filaments can be clearly found in the secondary jet (splash up). As shown in figure 7, these streamwise vortex are counter-rotating vortex pairs which can push the interface up and down and cause the interface deformation. Streamwise vortex filaments can also be seen underneath the entrained air tube in figure 6(c), which are also reported in Brucker *et al.* (2010) and Lubin & Glockner (2015).

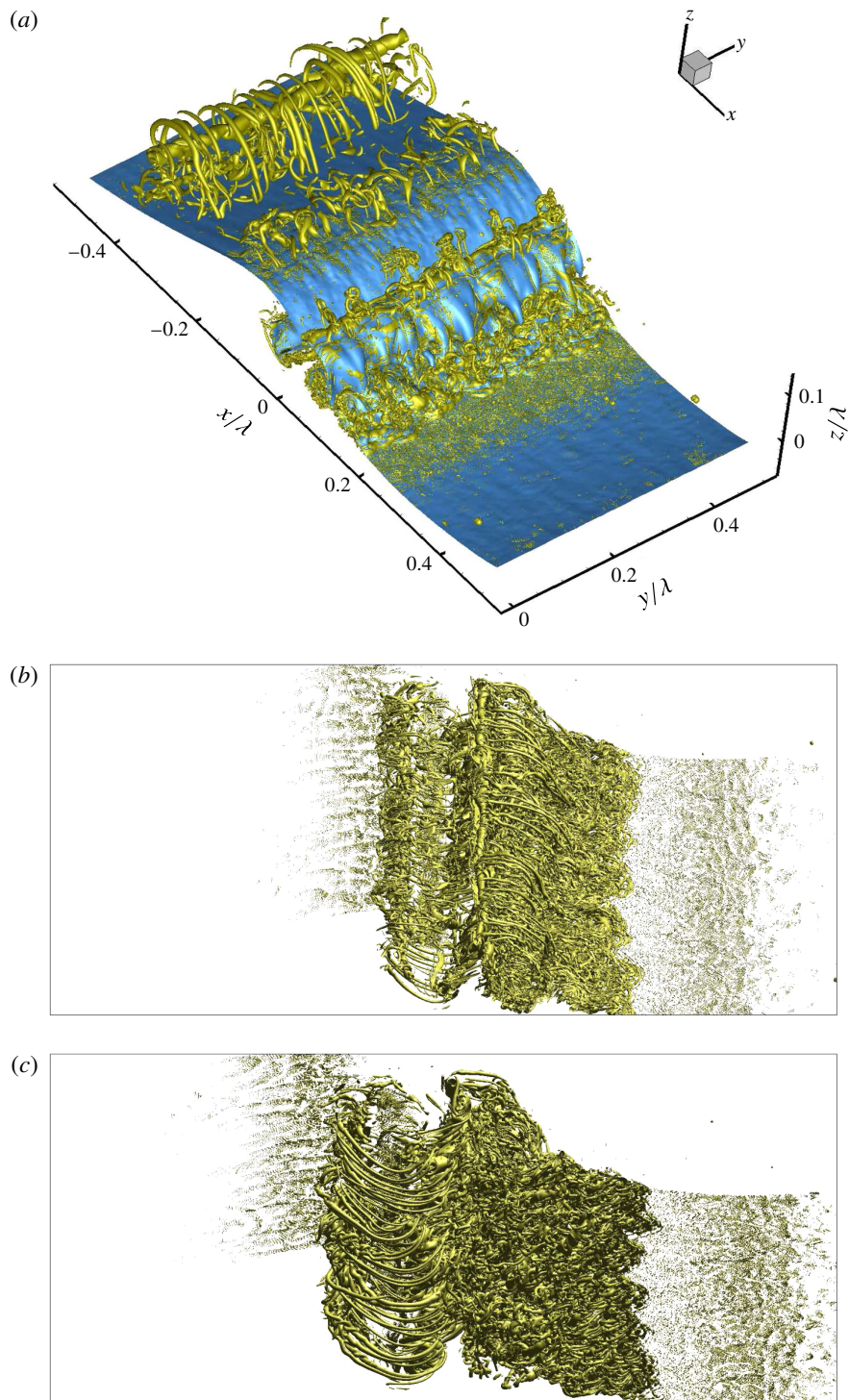


FIGURE 6. (Colour online) 3-D vortex structures of the plunging wave breaking at $t = 1.76$. (a) Perspective view of the Q isosurfaces in both air and water along with the interface; (b) top view of the Q isosurfaces in water phase; (c) bottom view of the Q isosurfaces in water phase.

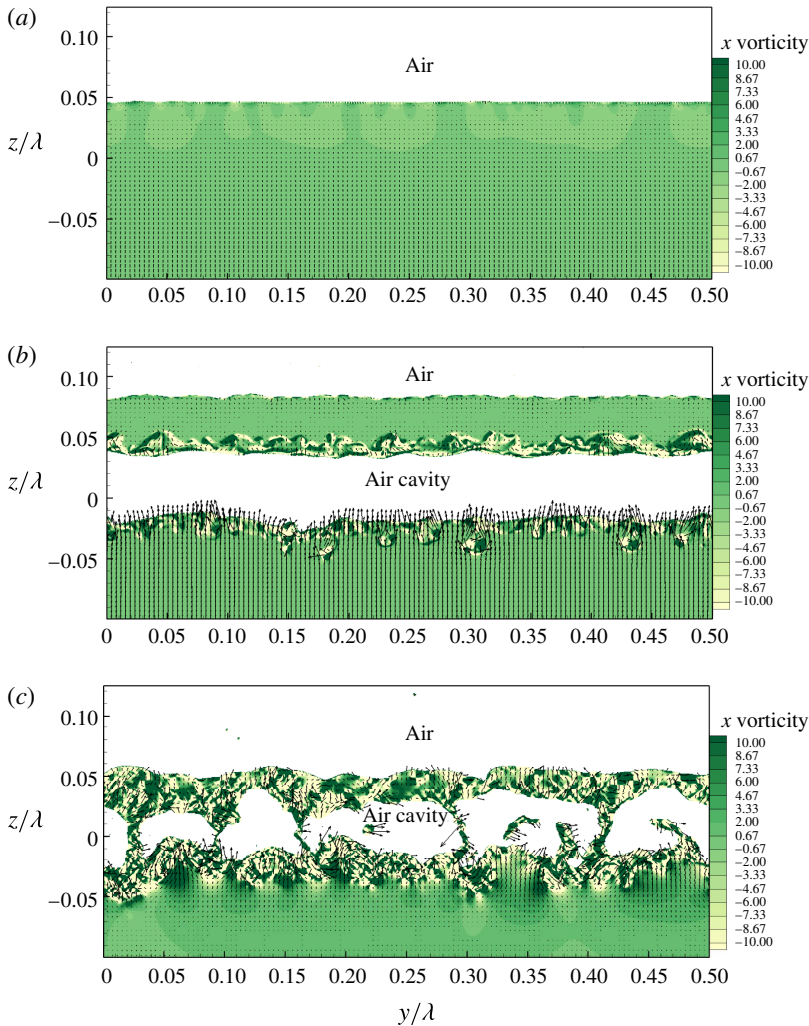


FIGURE 7. (Colour online) Cross-section velocity vector field and vortices (secondary flow field with the subtraction of mean vertical velocity for all the locations). (a) $x/\lambda = -0.25$; (b) $x/\lambda = -0.05$; (c) $x/\lambda = 0.05$.

The analysis of the instabilities in plunging wave breaking is difficult since many complex processes and phenomena are involved. The interface deformation also depends on the combined effect of gravity, surface tension and turbulence (Brocchini & Peregrine 2001). In an experimental study by Gui, Yoon & Stern (2014a,b), the instabilities for free-surface flow over a bump in a shallow water flume were investigated. The observed wavy gap flow exhibits jet-like velocity profiles, which is most relevant to the Görtler type centrifugal instability for convex curvature. The velocity profiles at several streamwise locations in the streamwise central plane are shown in figure 8. The detailed velocity profiles in the jet of the plunging wave breaking can be sufficiently resolved due to the high spatial resolution. According to the Görtler inviscid instability theory (Saric 1994), a flow is stable if the velocity magnitude increases with distance away from the wall for a convex curvature. The

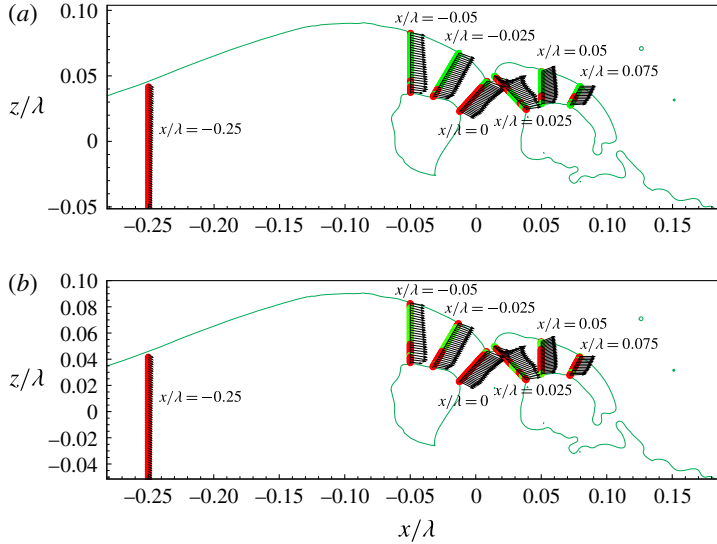


FIGURE 8. (Colour online) Velocity profiles in the jet at $y/\lambda = 0.25$. (a) Görtler inviscid instabilities; (b) Rayleigh instabilities. Red: stable; green: unstable.

stability criterion is $d(V_\theta)^2/dr > 0$, where r is the radius in the polar coordinate system with origin at the centre of curvature of the flow boundary, and V_θ is tangential velocity component. The Rayleigh inviscid stability requires that the angular momentum increases radially outward from the wall, i.e. the radial derivative of the circulation $(rV_\theta)^2$ must increase with the radius from the centre of the curvature, $d(rV_\theta)^2/dr > 0$. As shown in figures 8 and 9, in the upstream at $x/\lambda = -0.25$, the flow is stable, whereas in the wave breaking region, the Görtler stability criterion is violated in most locations and the Rayleigh stability criterion is broken only in small regions. Therefore, the breaking wave instabilities are likely mainly due to Görtler type centrifugal instability. It should be noted that only a brief discussion of the instability analysis is given above. More detailed analysis of the wave breaking instability is out of the scope of the present paper.

3.3. Air entrainment and spray formation

In plunging breaking waves, air can be entrained by several mechanisms, such as air tube entrapment and jet impact, entrapment by forward splash, backward-splash entrainment and turbulent entrainment, as discussed in Kiger & Duncan (2012). These air entrainment mechanisms are reproduced in the present simulation in greater detail due to the high grid resolution. Air entrainment processes are shown in figure 10 corresponding to the main air entrainment mechanisms given in Kiger & Duncan (2012). Figure 10(a–d) shows the plunging jet impact process during which an air tube is trapped. The entrapment of the air tube is the most clear and obvious air entrainment mechanism in plunging breaking waves. Air is also dragged into water when the jet hits the wave trough where very small bubbles are created at the jet impact site, as clearly shown in figure 10(a–d). Air is further entrapped as the forward splashes impact the trough surface, as shown in figure 10(e–h). Figure 10(i–l) shows the air entrainment between the backside of the rising splash and the original

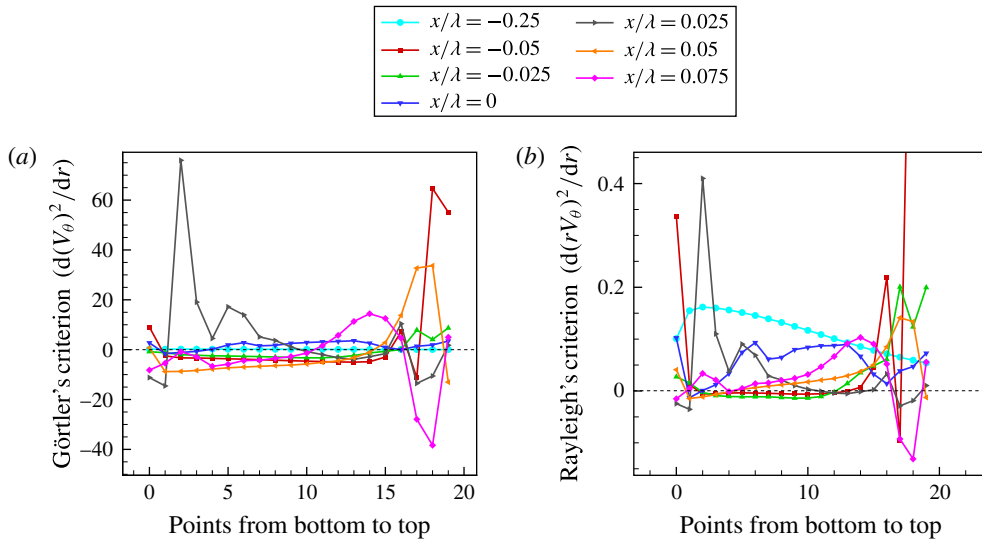


FIGURE 9. (Colour online) Intability criterion in the jet at $y/\lambda = 0.25$. (a) Görtler inviscid criterion; (b) Rayleigh inviscid criterion.

plunging jet. Air entrainment in the splash and turbulent wave breaking regions when the liquid ligament and droplets are formed and impact is shown in figure 10(m–p).

Once the jet tip touches the trough surface, splash up initiates and develops into a spray region with small droplets, as shown in figure 10(a–d). Detailed droplets and spray formation processes are given in figure 11. Figure 11(a–d) shows the liquid ligament formation and detachment from the stretched water surface. The detached ligament is then pinched off into droplets due to the surface tension effect, as shown in figure 11(e–h). This observation agrees with the spray formation mechanism explained by Longuet-Higgins (1995) for interface stretching, ligament fingering and droplet pinching off. A liquid jet is also formed and pinched off into droplets as the air bubble bursts into the air, as shown in figure 11(i–l). A detailed experimental study was conducted by Lhuissier & Villermaux (2012) focusing on the spray formation of a single bubble bursting. A new spray generation mechanism was observed in the experimental study by Veron *et al.* (2012) for sea spume droplet production at high wind speed. This break-up mechanism is driven by the wind, which is not applicable in the present study.

3.4. Bubble/droplet size distribution

The experimental study by (Deane & Stokes 2002) found that the bubble size distribution is controlled by two distinct mechanisms. Large bubbles ($r > 1.0$ mm) are determined by turbulent fragmentation and show a $-10/3$ power-law scaling, and smaller bubbles are created by jet and drop impact and show a $-3/2$ power-law scaling. For large bubbles, turbulent fragmentation and rising-bubble fragmentation are the two possible fragmentation mechanisms in wave breaking, as discussed in Soloviev & Lukas (2006). For turbulent fragmentation, a theoretical bubble size scaling equation was derived by Garrett, Li & Farmer (2000) which correlates bubble size spectra and energy dissipation rate for bubble break ups,

$$N(r) \propto Q\epsilon^{-1/3} r^{-10/3}, \tag{3.1}$$

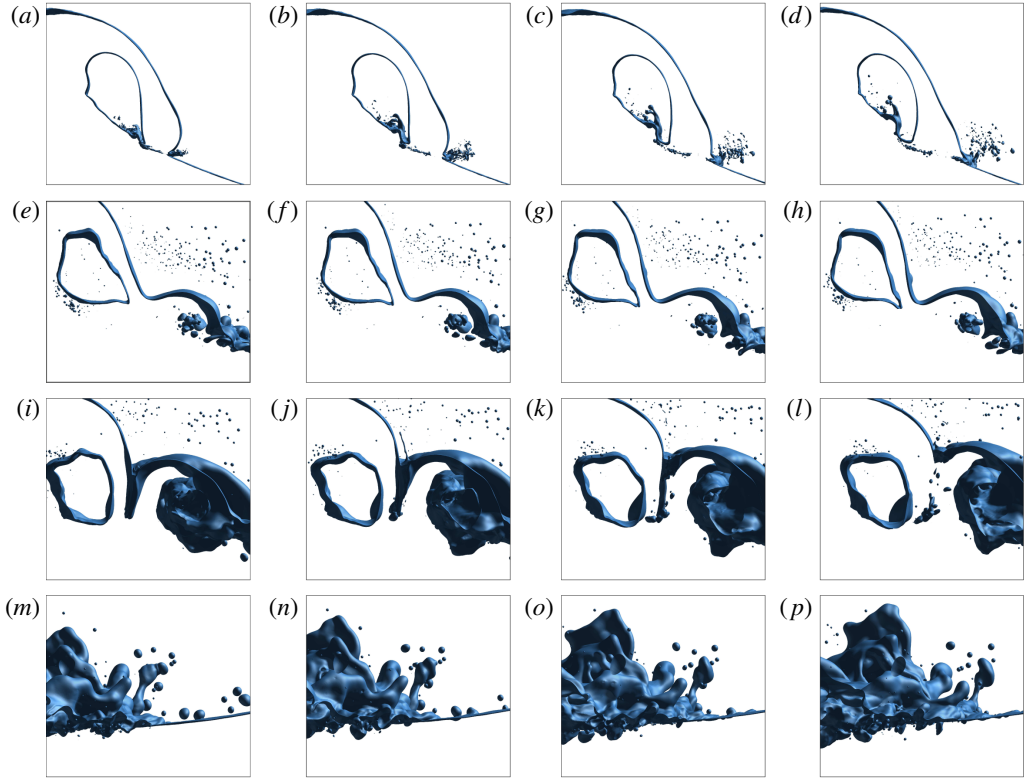


FIGURE 10. (Colour online) Air entrainment process. (a–d) Jet impact; (e–h) splash impact; (i–l) backward splash; (m–p) splash and turbulent regions. Time interval between images from left to right, $\Delta t = 0.01$ for (a–h); $\Delta t = 0.02$ for (i–p).

where $N(r)$ is the number of bubbles per μm radius increment per m^3 , Q is the air volume entrained per volume of water per second, ϵ is the energy dissipation rate and r is bubble radius. Turbulent fragmentation will cease when the bubble radius is less than the Hinze scale α_H , which is defined as (Deane & Stokes 2002),

$$\alpha_H = 2^{-8/5} \epsilon^{-2/5} (\sigma We_c / \rho_w)^{3/5}, \quad (3.2)$$

where σ is surface tension and We_c is the critical Weber number, which is chosen as $We_c = 4.7$. Bubbles smaller than the Hinze scale are stabilized by surface tension, and the process of turbulent fragmentation is believed to be less important. Deane & Stokes (2002) presented a scaling equation for small bubbles following the dimensional analysis by Garrett *et al.* (2000),

$$N(r) \propto Q(\sigma / \rho_w)^{-3/2} v^2 r^{-3/2}, \quad (3.3)$$

where v is the jet velocity. Rising-bubble fragmentation is characterized by the rise velocity w_b and collective interactions of rising bubbles. Soloviev & Lukas (2006) proposed a scaling equation based on the dimensional analysis for the bubble fragmentation dominated by buoyancy forces,

$$N(r) \propto Q w_b^{-1} r^{-3}. \quad (3.4)$$

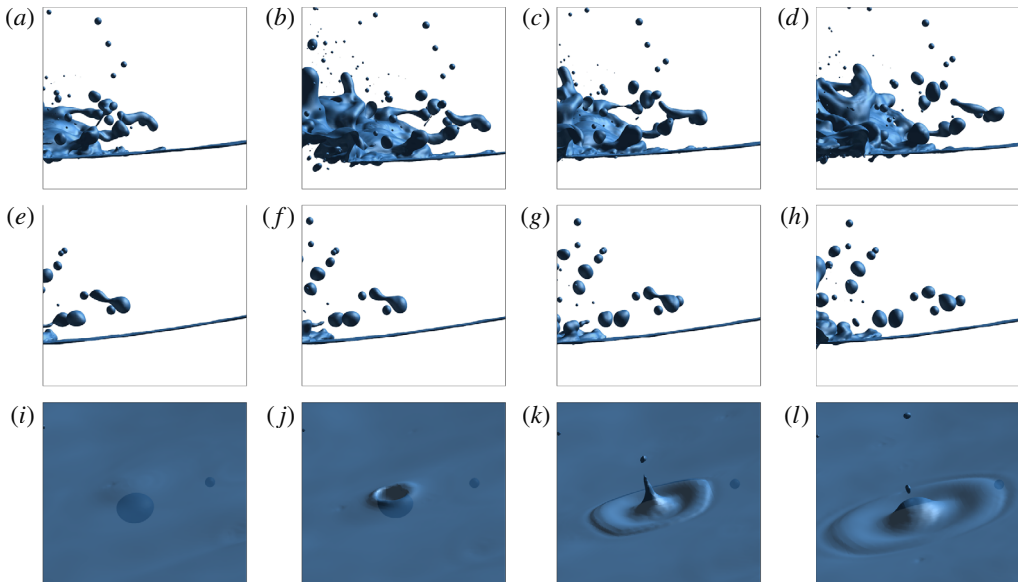


FIGURE 11. (Colour online) Droplets and spray formation. (a–d) Ligament detachment; (e–h) droplet break up; (i–l) bubble burst into air. Time interval between images from left to right, $\Delta t = 0.01$ for (a–h); $\Delta t = 0.02$ for (i–l).

The above -3 power law (3.4) is close to the $-10/3$ power law (3.1), and the former does not contain the energy dissipation rate ϵ .

Figure 12 shows the bubble size distributions for simulations on the three grids at different time instants along with the time averaged results. The number of bubbles is averaged over the active wave breaking period from $t = 1.44$ to $t = 3.25$ (total of 182 time instants) for the coarse and medium grids and from $t = 1.48$ to $t = 2.49$ (total of 102 time instants) for the fine grid. Simulation on the fine grid is terminated when the entrained air cavity collapses in order to save computational resources. The time average of bubble numbers is similar to those in experimental studies (Deane & Stokes 2002; Mori & Kakuno 2008; Tavakolinejad 2010) except that an additional average was also made over the experimental runs. The instantaneous bubble size distribution shows that most bubbles generated at the early wave breaking stages are small and larger bubbles can be found in the later wave breaking stages. This agrees with the experimental observations (Deane & Stokes 2002). The instantaneous bubble size distribution shows clear power-law scaling for small bubbles that is similar to the time-averaged scaling but the data are sparse for the large bubbles, which is also discussed in the experimental study of Mori & Kakuno (2008). For the large bubbles, the time averaged bubble size distribution shows -3.25 , -2.93 and -3.0 power-law scaling for the coarse, medium and fine grids, respectively. These values are close to and in the range of the experimental value -3.33 of Deane & Stokes (2002) for large bubbles. The relative errors of the values also decrease with grid refinement and show grid convergence. For small bubbles, the time-averaged bubble size distribution shows -1.82 and -1.46 power-law scaling for the medium and fine grids, respectively, the latter shows excellent agreement with the experimental measurement -1.50 (Deane & Stokes 2002). It should be noted that there is not sufficient data for the scaling of small bubbles on the coarse grid. Figure 12(d) shows the time averaged bubble size

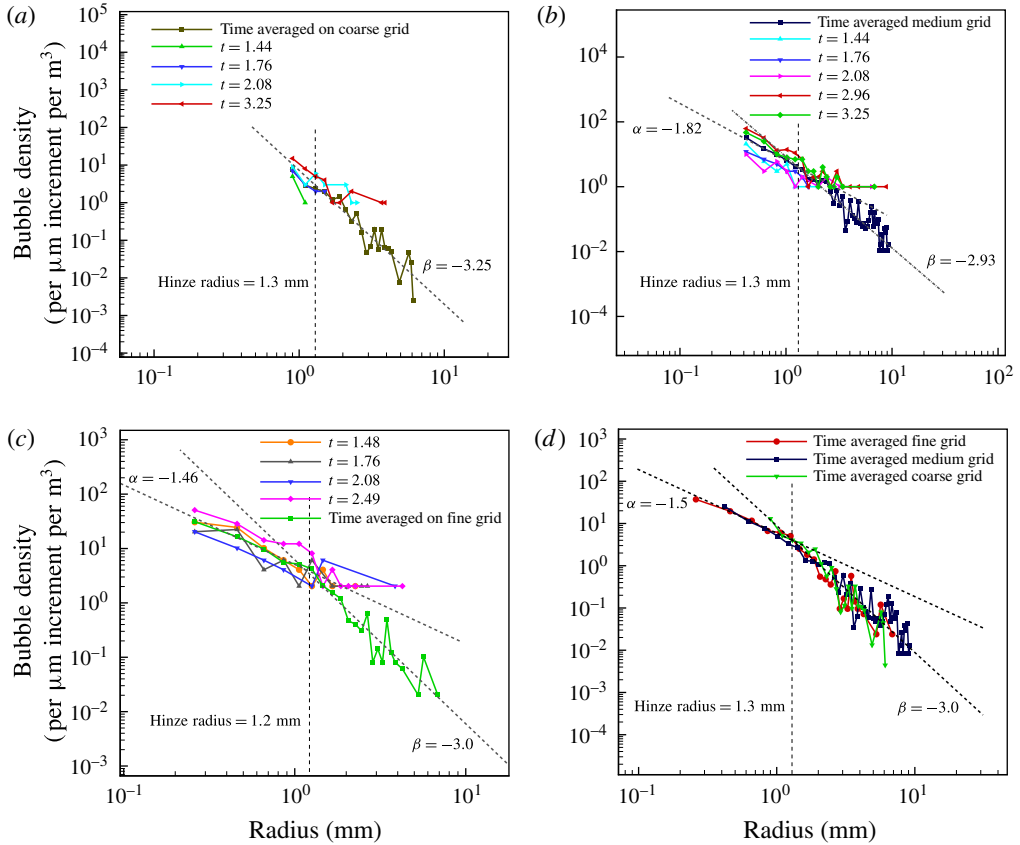


FIGURE 12. (Colour online) Instantaneous and time-averaged bubble size distribution. (a) Coarse grid; (b) medium grid; (c) fine grid; (d) time-averaged results of three grids.

distribution of the three grids including two reference lines of $\alpha = -1.5$ and $\beta = -3.0$ for the small and large bubbles, respectively, and the size distribution of small and large bubbles matches the two lines very well. It should be noted that for the large bubbles, the time-averaged size distribution shows scattered values. This can also be seen in the experimental results (Loewen *et al.* 1996; Deane & Stokes 2002; Mori & Kakuno 2008; Tavakolinejad 2010).

The experimental measurement of Deane & Stokes (2002) is consistent with the theoretical scaling (3.1) for the large bubbles. The slopes for large bubbles of the simulations are slightly less than the experimental and the theoretical values. This is probably due to the fact that the flows in the present simulations are not as violent as the experiments. Therefore, for large bubbles, turbulent fragmentation may not be dominant when compared to the rising-bubble fragmentation. It is clear that the scaling of large bubbles in the present simulations is much closer to the theoretical prediction (3.4). The small bubble size distribution of the simulation on the fine grid matches the $-3/2$ scaling for small bubbles (3.3), but the dependence on the jet velocity v is not tested, which needs further investigation.

As discussed in Deane & Stokes (2002), the bubble size spectra are separated by the Hinze scale (about 1.0 mm). Bubbles larger than the Hinze scale are due to turbulent fragmentation and sheared flow, and bubbles smaller than the Hinze scale

are stabilized by surface tension. As shown in figure 12, the Hinze radius of the present simulations is approximately 1.2–1.3 mm (visually obtained from the figures), which is close to the experimental value of 1.0 mm (Deane & Stokes 2002). To evaluate the Hinze scale using (3.2), the energy dissipation rate ϵ is needed, which can be estimated from the dissipation rate per unit length of the crest ϵ_l (Duncan 1981; Deane & Stokes 2002; Drazen, Melville & Lenain 2008),

$$\epsilon_l = b\rho_w c^5/g, \quad (3.5)$$

where b is the breaking parameter and c is the wave phase speed. According to the study by Drazen *et al.* (2008), b can be determined by $b = \beta(hk)^{5/2}$, where h is the height of the breaking region as shown in figure 1, k is the wavenumber and β is a parameter of $O(1)$. For the present simulations, the calculated wave breaking parameter b is 0.20 with $h = 0.03$ m, $k = 2\pi/\lambda$ and β chosen as 0.5. The dissipation rate per unit length of the crest is $\epsilon_l = 2.35$ W m⁻¹ with $c = 0.65$ m s⁻¹. The corresponding energy dissipation rate ϵ will be 6.6 W kg⁻¹ assuming the energy dissipated in the wave breaking region is within a radius $r = h/2.0$, following the experimental study of (Deane & Stokes 2002). It is clear that the wave breaking strength is less than the experiment (Deane & Stokes 2002) where the dissipation rate $\epsilon = 13$ W kg⁻¹. Substitution of the dissipation rate ϵ into (3.2) yields the Hinze radius $\alpha_H = 1.28$ mm, which is in good agreement with the Hinze scale observed in figure 12.

Figure 13 shows time-averaged droplet size distribution in the spray of the three simulations, along with the experimental results from the studies by Lhuissier & Villermaux (2012), Veron *et al.* (2012) and Towle (2014), which are fitted by a -4.5 power scaling function. The simulation results match the experimental measurement of Veron *et al.* (2012) very well. For droplets with $r > 0.4$ mm, the results of the present simulations and the experiment (Veron *et al.* 2012) also match the experimental data in Towle (2014). The data of the present simulations are not sufficient to compare with the results of Lhuissier & Villermaux (2012), because all the drops measured in the experiments are smaller than those resolved in the simulations. The results of Lhuissier & Villermaux (2012) agree well with those of Veron *et al.* (2012) for droplets with $r > 0.24$ mm. Following the dimensional analysis given in Garrett *et al.* (2000) and Deane & Stokes (2002), a scaling equation for the droplet size distribution is,

$$N(r) \propto u^{-1}(\sigma/\rho_w)^{1/2}r^{-9/2}, \quad (3.6)$$

where u is the jet velocity in the spray. Surface tension is included in the above equation because the radii of the droplets observed in the present simulations and experiments (Veron *et al.* 2012; Towle 2014) are mostly $r < 4$ mm. The -4.5 power-law scaling for the droplet size distribution is in good agreement with present simulations and the experiments. It is interesting to note that, although the spray formation mechanisms of these experimental studies and present simulations are different, which include sea spray spume drops due to high wind speed (Veron *et al.* 2012), plunging wave breaking (Towle 2014) and single bubble bursting (Lhuissier & Villermaux 2012), the drop size follows a similar power-law scaling for drops of the same size. Detailed analysis for the physics of drop size scaling is needed, which will be explored in future work.

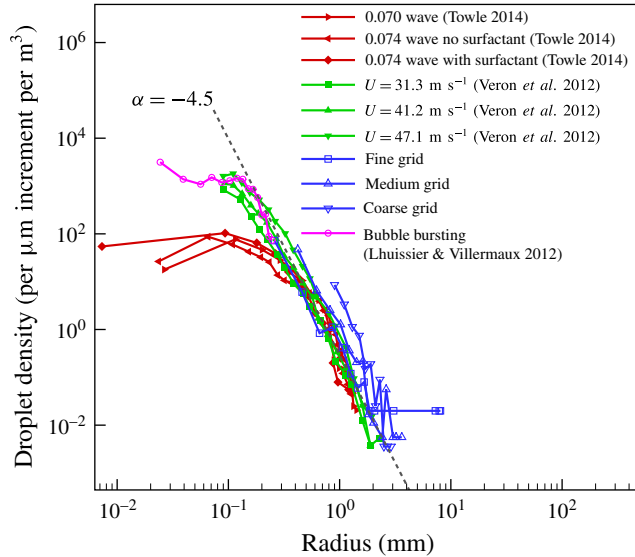


FIGURE 13. (Colour online) Drop size distribution.

4. Conclusions

Numerical simulations of wave breaking were conducted using billions of grid points in order to resolve the bubbles/droplets in breaking waves at the scale of hundreds of micrometres. The predictive capability of the computer code for the bubble/droplet size distribution was validated and the wave breaking processes, 3-D spanwise interface structures and air entrainment and spray formation were also investigated. The overall wave breaking process is in very good agreement with those reported in the literature. The 3-D spanwise interface structures and streamwise vortex filaments are identified and briefly analysed. It is speculated that the Görtler type centrifugal instability is more relevant to the wave breaking instabilities, which needs further detailed investigation. Detailed air entrainment and spray formation processes are shown. The air entrainment mechanisms of plunging wave breaking are shown with more details including primary jet impact, forward splash impact, backward-splash impact and splashes and droplets impacting in the turbulent regions. The spray formation processes of wave breaking include liquid interface stretching, ligament fingering and droplet pinching off. Droplets and jets are also formed when the air bubble bursts into the air. A new spray generation mechanism was observed in the experiments for sea spume droplet production at high wind speed, which is not applicable in the present study.

The instantaneous and time-averaged bubble size distributions of the simulations show power-law scaling. The time-averaged bubble size distribution for the coarse grid shows a -3.25 power scaling for the large bubbles. For the medium grid, it shows two power-law scaling with slopes of -1.82 and -2.93 for the small and large bubbles, respectively. As for the fine grid, the slopes of time-averaged scaling are -1.46 and -3.0 for small and large bubbles, respectively. These values are close to the experimental results and theoretical values. The observed Hinze scale from the bubble size spectra is $1.2\text{--}1.3 \text{ mm}$, which also agrees with experiment. The droplet size distribution also shows power-law scaling and compares well with the experimental measurements. A power-law scaling of -4.5 correlation is given

for the droplet size distribution. It is interesting to note that the drop size follows a similar power-law scaling for drops of the same size, even though the spray formation mechanisms are different.

The present study is, for the first time, able to resolve the bubbles/droplets at a scale of 0.3 mm in breaking waves and to capture the Hinze scale via numerical simulations. To achieve this, a high-fidelity computational tool has been employed with billions of grid points and a significant amount of computational resources used. The simulation results provide useful scientific data sets and insights for the wave breaking phenomena and a database for future analysis of bubble dynamics including break up and coalescence. Simulations on even finer grids can be considered to investigate and analyse the scaling mechanisms of small bubbles/droplets (at a scale down to 0.1 mm) if additional computational resources are available for such future work. It is believed that with the advancements in HPC and parallel computing technologies, the total CPU hours needed will be reduced and simulations at the scale of tens of or several micrometres are feasible in the near future.

Acknowledgements

This research was sponsored by the Office of Naval Research (ONR) under grant N000141-01-00-1-7, under the administration of Drs T. Fu and K.-H. Kim. The simulations were performed at the Department of Defense (DoD) Supercomputing Resource Centers (DSRCs) through the High Performance Computing Modernization Program (HPCMP). The authors would like to give special thanks to the ONR, Dr S. Harper, Dr R. Joslin, and Ms O. Murray for the help on the High Priority Queue.

Supplementary movie

Supplementary movie is available at <http://dx.doi.org/10.1017/jfm.2016.87>.

REFERENCES

- ANDREAS, E. L. 1998 A new sea spray generation function for wind speeds up to 32 m s^{-1} . *J. Phys. Oceanogr.* **28**, 2175–2184.
- AULISA, E., MANSERVISI, S., SCARDOVELLI, R. & ZALESKI, S. 2003 A geometrical area-preserving volume-of-fluid advection method. *J. Comput. Phys.* **192**, 355–364.
- BROCCHINI, M. & PEREGRINE, D. H. 2001 The dynamics of strong turbulence at free surfaces. Part 1. Description. *J. Fluid Mech.* **449**, 225–254.
- BRUCKER, K. A., O'SHEA, T. T., DOMMERMUTH, D. G. & ADAMS, P. 2010 Three-dimensional simulations of deep-water breaking waves. In *28th Symposium on Naval Hydrodynamics, Pasadena, CA*, U.S. Office of Naval Research (ONR).
- CARTMILL, J. & SU, M. 1993 Bubble size distribution under saltwater and freshwater breaking waves. *Dyn. Atmos. Oceans* **20**, 25–31.
- CHEN, G., KHARIF, C., ZALESKI, S. & LI, J. 1999 Two-dimensional Navier–Stokes simulation of breaking waves. *Phys. Fluids* **11**, 121–133.
- CHOI, H. & MOIN, P. 1994 Effects of the computational time step on numerical solutions of turbulent flow. *J. Comput. Phys.* **113**, 1–4.
- CLIFT, R., GRACE, J. R. & WEBBER, M. E. 1978 *Bubbles, Drops, and Particles*. Academic.
- DEANE, G. B. & STOKES, M. D. 2002 Scale dependency of bubble creation mechanisms in breaking waves. *Nature* **418**, 839–844.
- DERAKHTI, M. & KIRBY, J. T. 2014 Bubble entrainment and liquid–bubble interaction under unsteady breaking waves. *J. Fluid Mech.* **761**, 464–506.

- DRAZEN, D. A., MELVILLE, W. K. & LENAIN, L. 2008 Inertial scaling of dissipation in unsteady breaking waves. *J. Fluid Mech.* **611**, 307–332.
- DUNCAN, J. H. 1981 An experimental investigation of breaking waves produced by a towed hydrofoil. *Proc. R. Soc. Lond. A* **377** (1770), 331–348.
- FALGOUT, R. D., JONES, J. E. & YANG, U. M. 2006 The design and implementation of hypre, a library of parallel high performance preconditioners. In *Numerical Solution of Partial Differential Equations on Parallel Computers* (ed. A. Bruaset & A. Tveito), Lecture Notes in Computational Science and Engineering, vol. 51, pp. 267–294. Springer.
- GARRETT, C., LI, M. & FARMER, D. 2000 The connection between bubble size spectra and energy dissipation rates in the upper ocean. *J. Phys. Oceanogr.* **30**, 2163–2171.
- GUI, L., YOON, H. & STERN, F. 2014a Experimental and theoretical investigation of instabilities for flow over a bump in a shallow water flume with steady downstream wave train. *Tech. Rep.* 487. IIHR, The University of Iowa.
- GUI, L., YOON, H. & STERN, F. 2014b Techniques for measuring bulge-car pattern of free surface deformation and related velocity distribution in shallow water flow over a bump. *Exp. Fluids* **55** (4), 1721.
- HERRMANN, M. 2010 A parallel Eulerian interface tracking/Lagrangian point particle multi-scale coupling procedure. *J. Comput. Phys.* **229** (3), 745–759.
- HINZE, J. O. 1955 Fundamentals of the hydrodynamic mechanism of splitting in dispersion processes. *AIChE J.* **1** (3), 289–295.
- IAFRATI, A. 2009 Numerical study of the effects of the breaking intensity on wave breaking flows. *J. Fluid Mech.* **622**, 371–411.
- IAFRATI, A. 2010 Air–water interaction in breaking wave events: quantitative estimates of drops and bubbles. In *28th Symposium on Naval Hydrodynamics, Pasadena, CA*, U.S. Office of Naval Research (ONR).
- JEONG, J. & HUSSAIN, F. 1995 On the identification of a vortex. *J. Fluid Mech.* **285**, 69–94.
- JIANG, G.-S. & SHU, C.-W. 1996 Efficient implementation of weighted ENO schemes. *J. Comput. Phys.* **126** (1), 202–228.
- KANG, D., GHOSH, S., REINS, G., KOO, B., WANG, Z. & STERN, F. 2012 Impulsive plunging wave breaking downstream of a bump in a shallow water flume. Part I. Experimental observations. *J. Fluids Struct.* **32**, 104–120.
- KIGER, K. T. & DUNCAN, J. H. 2012 Air entrainment mechanisms in plunging jets and breaking waves. *Annu. Rev. Fluid Mech.* **44**, 563–596.
- KOO, B., WANG, Z., YANG, J. & STERN, F. 2012 Impulsive plunging wave breaking downstream of a bump in a shallow water flume. Part II. Numerical simulations. *J. Fluids Struct.* **32**, 121–134.
- LEONARD, B. P. 1979 A stable and accurate convective modelling procedure based on quadratic upstream interpolation. *Comput. Meth. Appl. Mech. Engng* **19** (1), 59–98.
- LHUISSIER, H. & VILLERMAUX, E. 2012 Bursting bubble aerosols. *J. Fluid Mech.* **696**, 5–44.
- LI, X., ARIENTI, M., SOTERIOU, M. C. & SUSSMAN, M. M. 2010 Towards an efficient, high-fidelity methodology for liquid jet atomization computations. *AIAA Paper* 2010-210.
- LOEWEN, M. R., ODOR, M. A. & SKAFEL, M. G. 1996 Bubbles entrained by mechanically generated breaking waves. *J. Geophys. Res.* **101**, 20759–20820.
- LONGUET-HIGGINS, M. 1995 On the disintegration of the jet in a plunging breaker. *J. Phys. Oceanogr.* **25**, 2458–2462.
- LUBIN, P. & GLOCKNER, S. 2015 Numerical simulations of three-dimensional plunging breaking waves: generation and evolution of aerated vortex filaments. *J. Fluid Mech.* **767**, 364–393.
- LUBIN, P., VINCENT, S., ABADIE, S. & CALTAGIRONE, J. P. 2006 Three-dimensional large eddy simulation of air entrainment under plunging breaking waves. *Coast. Engng* **53**, 631–655.
- MORI, N. & KAKUNO, S. 2008 Aeration and bubble measurements of coastal breaking waves. *Fluid Dyn. Res.* **40** (7–8), 616–626.
- SARIC, W. S. 1994 Görtler vortices. *Annu. Rev. Fluid Mech.* **26**, 379–409.

- SARUWATARI, A., WATANABE, Y. & INGRAM, D. M. 2009 Scarifying and fingering surfaces of plunging jets. *Coast. Engng* **56** (1112), 1109–1122.
- SCARDOVELLI, R. & ZALESKI, S. 2003 Interface reconstruction with least-square fit and split Eulerian–Lagrangian advection. *Intl J. Numer. Meth. Fluids* **41**, 251–274.
- SOLOVIEV, A. & LUKAS, R. 2006 *The Near-Surface Layer of the Ocean: Structure, Dynamics and Applications*. Springer.
- SUH, J., YANG, J. & STERN, F. 2011 The effect of air–water interface on the vortex shedding from a vertical circular cylinder. *J. Fluids Struct.* **27**, 1–22.
- TAVAKOLINEJAD, M. 2010 Air bubble entrainment by breaking bow waves simulated by a $2d + t$ technique. PhD thesis, University of Maryland.
- TOWLE, D. M. 2014 Spray droplet generation by breaking water waves. Master’s thesis, University of Maryland.
- VERON, F., HOPKINS, C., HARRISON, E. L. & MUELLER, J. A. 2012 Sea spray spume droplet production in high wind speeds. *Geophys. Res. Lett.* **39** (16), 116602.
- WANG, Z., SUH, J., YANG, J. & STERN, F. 2012b Sharp interface LES of breaking waves by an interface piercing body in orthogonal curvilinear coordinates. *AIAA Paper* 2012-1111.
- WANG, Z., YANG, J., KOO, B. & STERN, F. 2009a A coupled level set and volume-of-fluid method for sharp interface simulation of plunging breaking waves. *Intl J. Multiphase Flow* **35**, 227–246.
- WANG, Z., YANG, J. & STERN, F. 2009b An improved particle correction procedure for the particle level set method. *J. Comput. Phys.* **228** (16), 5819–5837.
- WANG, Z., YANG, J. & STERN, F. 2012a High-fidelity simulations of bubble, droplet, and spray formation in breaking waves. *HPC Insights*, Fall Issue, 5–7.
- WANG, Z., YANG, J. & STERN, F. 2012c A new volume-of-fluid method with a constructed distance function on general structured grids. *J. Comput. Phys.* **231**, 3703–3722.
- WANG, Z., YANG, J. & STERN, F. 2012d A simple and conservative operator-splitting semi-Lagrangian volume-of-fluid advection scheme. *J. Comput. Phys.* **231**, 4981–4992.
- WATANABE, Y. & SAEKI, H. 2002 Velocity field after wave breaking. *Intl J. Numer. Meth. Fluids* **39**, 607–637.
- WATANABE, Y., SAEKI, H. & HOSKING, R. 2005 Three-dimensional vortex structures under breaking waves. *J. Fluid Mech.* **545**, 291–328.
- YANG, J., BHUSHAN, S., SUH, J., WANG, Z., KOO, B., SAKAMOTO, N. & XING, T. 2008 Large-eddy simulation of ship flows with wall-layer models on cartesian grids. In *27th Symposium on Naval Hydrodynamics, Seoul, Korea*, U.S. Office of Naval Research (ONR).
- YANG, J. & STERN, F. 2007 A sharp interface method for two-phase flows interacting with moving bodies. *AIAA Paper* 2007-4578.
- YANG, J. & STERN, F. 2009 Sharp interface immersed-boundary/level-set method for wave–body interactions. *J. Comput. Phys.* **228**, 6590–6616.
- ZHOU, Z., SANGERMANO, J., HSU, T.-J. & TING, F. C. K. 2014 A numerical investigation of wave-breaking-induced turbulent coherent structure under a solitary wave. *J. Geophys. Res.* **119** (10), 6952–6973.